Phosphatidylserine and GTPase activation control Cdc42 nanoclustering to counter dissipative diffusion

Elodie Sartorel[a,†], Caner Ünlü[a,†,‡], Mini Jose[a,§], Aurélie Massoni-Laporte[a], Julien Meca[a], Jean-Baptiste Sibarita[b,c], and Derek McCusker[a,*]
[a]Université Bordeaux, CNRS, UMR 5095, European Institute of Chemistry and Biology, Pessac 33607, France;
[b]Université Bordeaux and [c]CNRS UMR 5297, Institut Interdisciplinaire de Neurosciences, Bordeaux 33077, France

ABSTRACT **The anisotropic organization of plasma membrane constituents is indicative of mechanisms that drive the membrane away from equilibrium. However, defining these mechanisms is challenging due to the short spatiotemporal scales at which diffusion operates. Here, we use high-density single protein tracking combined with photoactivation localization microscopy (sptPALM) to monitor Cdc42 in budding yeast, a system in which Cdc42 exhibits anisotropic organization. Cdc42 exhibited reduced mobility at the cell pole, where it was organized in nanoclusters. The Cdc42 nanoclusters were larger at the cell pole than those observed elsewhere in the cell. These features were exacerbated in cells expressing Cdc42-GTP, and were dependent on the scaffold Bem1, which contributed to the range of mobility and nanocluster size exhibited by Cdc42. The lipid environment, in particular phosphatidylserine levels, also played a role in regulating Cdc42 nanoclustering. These studies reveal how the mobility of a Rho GTPase is controlled to counter the depletive effects of diffusion, thus stabilizing Cdc42 on the plasma membrane and sustaining cell polarity.**

Monitoring Editor
Fred Chang
University of California, San Francisco

Received: Jan 22, 2018
Revised: Mar 12, 2018
Accepted: Apr 5, 2018

INTRODUCTION

Functional compartmentalization of the plasma membrane underlies essential cellular processes in diverse biological systems. For example, different Rho GTPases are localized adjacently on the plasma membrane, forming spatially patterned zones of activity during cytokinesis (Bastos *et al.*, 2012), polar body extrusion, and wound healing (Benink and Bement, 2005; Zhang *et al.*, 2008; Bement and von Dassow, 2014). Similarly, membrane trafficking compartments display an organized, annular conformation in neuronal synapses (Roos and Kelly, 1999; Wahl *et al.*, 2013), and during polarity establishment in budding yeast, where sites of endo- and exocytosis form a bull's-eye pattern on the plasma membrane (Jose *et al.*, 2013, 2015). Plasma membrane reorganization also accompanies T-cell receptor (TCR) engagement with antigen-presenting cells at the immunological synapse. Here, activated TCR forms a central supramolecular activation cluster, surrounded by adhesion proteins, kinases, and specific lipids (Monks *et al.*, 1998; Yokosuka *et al.*, 2008; Le Floc'h *et al.*, 2013). These diverse plasma membrane phenomena share a common underlying principle: all are highly dynamic cytoskeletal-driven processes controlled by Rho GTPases.

The activity of Rho GTPases is strongly influenced by their rate of activation and inactivation (Goryachev and Pokhilko, 2008), and the extent to which they diffuse on membranes (Giese *et al.*, 2015). Although we understand some of the GEF and GAP-mediated mechanisms that control Rho GTPase activity, even at atomic resolution (Rittinger *et al.*, 1997; Yu *et al.*, 2010), our understanding of the mechanisms that control the diffusion of Rho GTPases and their regulators on the plasma membrane of cells is less developed (Trimble and Grinstein, 2015). Theoretically, proteins and lipids diffuse on membranes down concentration gradients until they reach equilibrium and

This article was published online ahead of print in MBoC in Press (http://www.molbiolcell.org/cgi/doi/10.1091/mbc.E18-01-0051) on April 18, 2018.

[†]These authors contributed equally to this work.

Present addresses: [‡]Chemistry Department, Istanbul Technical University, Istanbul 34469, Turkey; [§]Centre for Neuroscience, Indian Institute of Science, Bangalore 560012, India.

*Address correspondence to: Derek McCusker (mccusker@iecb.u-bordeaux.fr).

Abbreviations used: AFIC, average fluorescence intensity of the cytosol; AFIP, average fluorescence intensity of the pole; CRIB, Cdc42 and Rac-interactive binding; *D*, instantaneous diffusion coefficient; EMCDD, electron-multiplying charge-coupled device; FRAP, fluorescence recovery after photobleaching; FWHM, full width at half maximum; HiLo, highly oblique imaging; IQR, interquartile range; MSD, mean square displacement; OD, optical density; PBS, phosphate-buffered saline; PC, phosphatidylcholine; PE, phosphatidylethanolamine; PS, phosphatidylserine; SC, synthetic complete; sptPALM, single-particle tracking photoactivation localization microscopy; TCR, T-cell receptor; TIRF, total internal reflection fluorescence microscopy; WT, wild type.

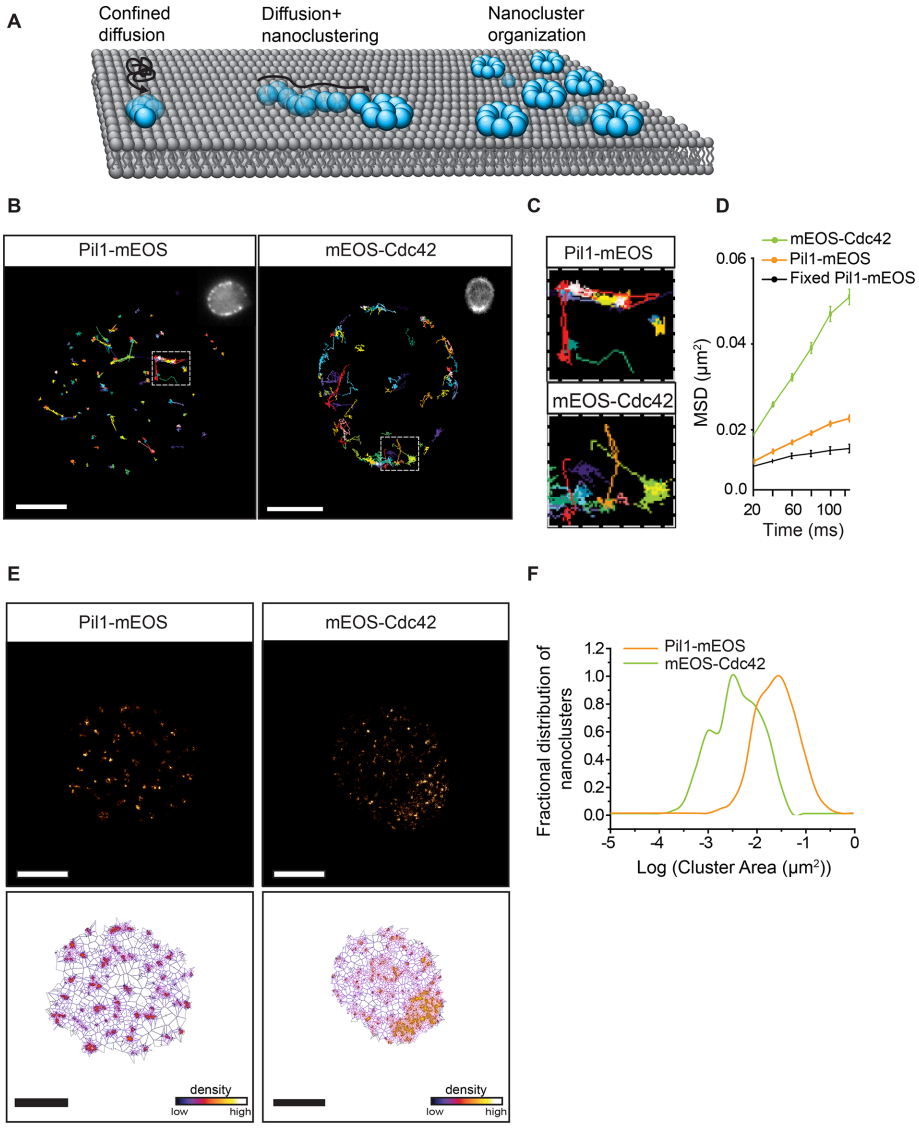

FIGURE 1: Heterogeneity in the organization and dynamics of peripheral plasma membrane proteins. (A) Modes of diffusive behavior and nano-organization amenable to sptPALM analysis. (B) High-density tracking of mEOS-Cdc42 and Pil1-mEOS in live WT cells computed by sptPALM. Scale bar: 2 μm. Different colored trajectories show individual mEOS-tagged proteins that were reconstructed from 20,000 images acquired at 20-ms intervals. Only trajectories longer than 10 frames are displayed. Insets show Pil1-mEOS and mEOS-Cdc42 after 491-nm laser excitation to identify global protein organization in a plane more sagittal to that used for spt acquisitions. (C) Zoom of the area of plasma membrane shown in the box in panel B. (D) Global average MSD curves of mEOS-Cdc42 ($N = 11$ cells, $n = 2608$ trajectories) and Pil1-mEOS ($N = 10$ cells, $n = 5515$ trajectories). Trajectories longer than six frames were analyzed. The MSD curve of a fixed sample is included as a control. (E) PALM image of Pil1-mEOS and mEOS-Cdc42 organization in fixed WT cells. The localization of each mEOS-tagged protein was detected from 32,000 to 40,000 images acquired at 20-ms intervals (top panels) and nanoclusters of mEOS-tagged proteins were analyzed by SR-Tesseler (bottom panels). Images display 4092 and 3457 localizations for Pil1-mEOS and mEOS-Cdc42, respectively. Note that it is necessary to zoom beyond 1200% to observe single protein localizations in the PDF. Scale bar: 2 μm. (F) Distribution of the log(Area(μm^2)) of mEOS-Cdc42 and Pil1-mEOS nanoclusters in fixed WT strains (Pil1-mEOS: $N = 10$ cells, $n = 589$ clusters; mEOS-Cdc42: $N = 10$ cells, $n = 625$ clusters).

are uniformly distributed. However, it is becoming apparent that the plasma membrane of cells rarely exhibits homogeneous distribution of its constituents, indicating the existence of mechanisms that drive the system away from equilibrium, countering the dissipative effects of diffusion (Rao and Mayor, 2014).

RESULTS AND DISCUSSION

To investigate the utility of high-density sptPALM to probe peripheral plasma membrane protein dynamics in budding yeast, we studied two proteins displaying high and low rates of diffusion: the GTPase Cdc42 and the eisosome protein Pil1 (Figure 1A;

The Rho GTPase Cdc42 in budding and fission yeast provides a powerful model system to identify these mechanisms. Cdc42 is asymmetrically localized on the plasma membrane at the cell pole, defining the polarity axis used for cell growth and division. Previous studies suggested that Cdc42 diffusion is reduced at the pole in vivo, compared with other regions of the membrane (Slaughter *et al.*, 2013; Bendezu *et al.*, 2015). Moreover, expression of active Cdc42 GTP constructs displayed slower recovery by fluorescence recovery after photobleaching (FRAP), reflecting slower diffusion of the active GTPase (Wedlich-Soldner *et al.*, 2004; Freisinger *et al.*, 2013; Bendezu *et al.*, 2015). This reduced diffusion of active Cdc42 might indicate the stabilization of Cdc42 at the pole, where it participates in polarity axis establishment. Thus, Cdc42 activation and its diffusion at the pole may be linked, predicting that mutants affecting Cdc42 activation may display altered rates of GTPase diffusion. The Cdc42 scaffold protein Bem1 plays a direct role in GTPase activation (Smith *et al.*, 2013; Rapali *et al.*, 2017). However, previous FRAP studies did not report gross differences in Cdc42 recovery in *bem1*Δ cells (Wedlich-Soldner *et al.*, 2004). A caveat to the interpretation of FRAP experiments is the ensemble nature of the measurements. Given that subpopulations of Cdc42 have been proposed to exist in the plasma membrane, displaying reduced diffusion at the pole and faster diffusion elsewhere (Slaughter *et al.*, 2013; Bendezu *et al.*, 2015), the mobility of the GTPase might be better appreciated if studied using single-particle tracking techniques, where different subpopulations displaying a range of diffusion characteristics can be directly monitored. This approach has been successfully employed in studies on other GTPases that are organized anisotropically, including Rac1, H-Ras, and K-Ras (Murakoshi *et al.*, 2004; Lin *et al.*, 2014; Das *et al.*, 2015). Here, we investigate the dynamics and organization of Cdc42 and the eisosome marker Pil1 on the plasma membrane using high-density single protein tracking combined with photoactivation localization microscopy (sptPALM; Manley *et al.*, 2008). Our results reveal the heterogeneous mobility displayed by plasma membrane proteins and indicate a key role for GTPase activation and the lipid environment in the dynamics and nanoscale organization displayed by Cdc42.

Walther *et al.*, 2006; Marco *et al.*, 2007; Manley *et al.*, 2008). Pil1 and Cdc42 were tagged with the photoconvertible mEOS fluorescent protein. These tagged versions of the proteins, expressed from their native promoter, served as the sole source of the proteins, unless stated otherwise in the text. Because *CDC42* is essential, the viability of the mEOS-tagged Cdc42 strain, when expressed from a CEN plasmid, or when integrated in the genome, indicates the retention of essential Cdc42 function (Supplemental Figure S1, A and B). Moreover, axial budding patterns, which are dependent upon Cdc42 (Adams *et al.*, 1990), were indistinguishable from wild-type cells when mEOS-Cdc42 was expressed as the sole source of the protein (Supplemental Figure S1C). Cell morphology during the cell cycle and after pheromone treatment was also indistinguishable from untagged control strains (Supplemental Figure S1D). In addition, the response of cells expressing integrated *mEOS-CDC42* to pheromone at a population level was indistinguishable from untagged control cells (Supplemental Figure S1E). Collectively, these results indicate that the mEOS-Cdc42 fusion protein supports essential and nonessential Cdc42 functions in cell polarity.

sptPALM was used to quantify the organization and dynamics of Pil1-mEOS and mEOS-Cdc42 in wild-type cells (Figure 1B). A low-power 405-nm laser induced the stochastic photoconversion of a subset of mEOS-tagged molecules, which were imaged by highly oblique illumination (HiLo) using a 561-nm laser (Tokunaga *et al.*, 2008). This approach provided a high mEOS signal-to-noise ratio on the plasma membrane and a low cytoplasmic background signal, which is evident in movies where it is difficult to delineate the interior of the cell due to the low cytoplasmic signal (Supplemental Movie 1). Thousands of single-particle trajectories were reconstructed from tens of thousands of localizations (Figure 1B), revealing heterogeneity in the diffusive properties of single proteins, ranging from immobile to highly diffusive (Figure 1C). In the analysis, tracks longer than six frames were analyzed. Pil1-mEOS exhibited considerable confinement, while occasionally displaying rapid, highly directed diffusion between protein clusters. Some confined molecules were juxtaposed to each other, suggesting that in *Saccharomyces cerevisiae*, a cohort of Pil1 may be organized in filaments in vivo, as reported in *Schizosaccharomyces pombe* (Figure 1C; Kabeche *et al.*, 2011). mEOS-Cdc42 was more dynamic than Pil1-mEOS, as reflected in mean square displacement (MSD) analysis. The mobility of Pil1-mEOS in live cells was quantified as the instantaneous diffusion coefficient, *D* (median *D*, 0.0061 $\mu m^2\ s^{-1}$ ± 0.00068), extracted by fitting the MSD curves, which was greatly reduced compared with mEOS-Cdc42 (median *D*, 0.022 $\mu m^2\ s^{-1}$ ± 0.0009; Figure 1D and Table 1). The organization of mEOS-Cdc42 and Pil1-mEOS in subdiffraction-limited clusters, which we refer to as nanoclusters, or eisosomes in the case of Pil1, became more evident when cells were fixed and imaged by PALM (Figure 1E). The nano-organization of the proteins was analyzed by SR-Tesseler (Levet *et al.*, 2015), in which single-molecule localizations are treated as seeds around which polygons are generated to build up a detailed cartography of molecular density. Pil1-mEOS was organized in nanoclusters, or eisosomes, that were larger, on average, than mEOS-Cdc42 nanoclusters, as reflected in the distribution of nanocluster sizes (median diameter of Pil1-mEOS nanoclusters, 105 nm ± 2 nm [SEM], vs. mEOS-Cdc42 nanoclusters, 67 nm ± 2 nm [SEM; Figure 1F]). The median value is provided rather than the mean because the nanocluster sizes were not normally distributed, as will be described below. The median diameter of Pil1 eisosomes that we report (105 nm) is consistent with a recent study, which measured Pil1-mKate2 in eisosomes of 101 by 71 nm (Bianchi *et al.*, 2018). However, the highly mobile pool of Pil1 that we observe during live cell imaging was not reported by Bianchi *et al.*, reflecting the higher rate of image acquisition in our sptPALM experiments. Collectively, our results illustrate the heterogeneity of the molecular organization and dynamics of plasma membrane proteins, and the amenability of these features to high-density sptPALM in yeast.

The spatial control of Cdc42 diffusion could contribute to cellular polarity by stabilizing the GTPase at the cell pole. Although such a mechanism has been inferred from ensemble measurements, it has not been observed directly (Orlando *et al.*, 2011; Slaughter *et al.*, 2013; Bendezu *et al.*, 2015). We reasoned that were such a mechanism to operate, it would likely involve Bem1, a scaffold involved in the regulation of Cdc42 activation and signaling (Smith *et al.*, 2013; Woods *et al.*, 2015; Rapali *et al.*, 2017). We therefore performed quantitative sptPALM analysis of mEOS-Cdc42 in wild-type and *bem1*Δ cells that were establishing a polarity axis (Figure 2A). The instantaneous diffusion coefficient, *D*, extracted from all MSD trajectories of wild-type cells was measured and found to be almost twofold lower at the pole compared with the nonpole (median *D* pole, 0.016 $\mu m^2\ s^{-1}$ ± 0.00098; median *D* nonpole, 0.027 $\mu m^2\ s^{-1}$ ± 0.00095; Figure 2B and Table 1). In contrast to our measurements in wild-type cells, *D* was more homogeneous over the entire cell, that is, pole and nonpole regions, in *bem1*Δ cells, despite the fact that these cells were also polarizing (median *D* pole, *bem1*Δ, 0.019 $\mu m^2\ s^{-1}$ ± 0.00089; median *D* nonpole, *bem1*Δ, 0.019 $\mu m^2\ s^{-1}$ ± 0.0011; Figure 2B and Table 1). These results suggest that Cdc42 activation and its reduced mobility are linked. Consistently, we also observed that the diffusion of mEOS-Cdc42-GTP produced by the *cdc42-Q61L* mutant was reduced even further than that of wild-type mEOS-Cdc42 at the cell pole (median *D* pole, *cdc42-Q61L*, 0.011 $\mu m^2\ s^{-1}$ ± 0.00125; median *D* nonpole, *cdc42-Q61L*, 0.015 $\mu m^2\ s^{-1}$ ± 0.00165; Figure 2B and Table 1). In these experiments, the expression of a wild-type copy of *CDC42* expressed from the *GAL1* promoter was repressed by adding dextrose to cells, enabling subsequent imaging of mEOS-cdc42-Q61L expressed from the *CDC42*

	D coefficient ($\mu m^2\ s^{-1}$)					
	Pole (median)	Nonpole (median)	SE values		No. of trajectories	
			Pole	Nonpole	Pole	Nonpole
*BEM*1 (WT) *mEOS-CDC42* (11 cells)	0.016	0.027	0.000988	0.000958	618	2607
*bem1*Δ *mEOS-CDC42* (11 cells)	0.019	0.019	0.000891	0.001119	1416	2198
W303 (WT) *mEOS-CDC42* (10 cells)	0.015	0.023	0.0013	0.0010	478	2671
W303 *mEOS-cdc42(Q61L)* (10 cells)	0.011	0.015	0.00125	0.00165	2015	750
PIL1-mEOS (10 cells)	0.0061		0.00068		5514	

TABLE 1: *D* coefficient values extracted from sptPALM data.

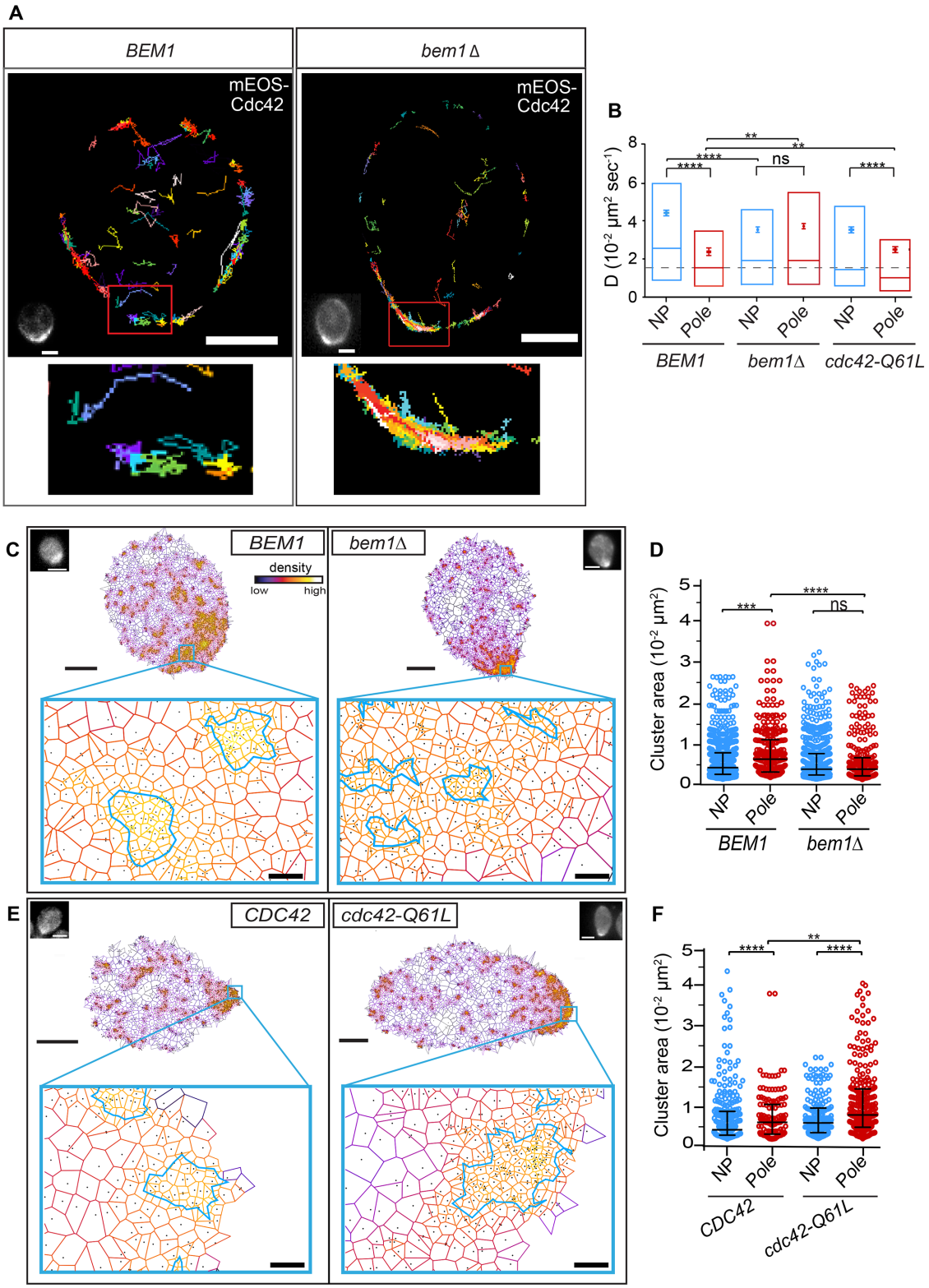

FIGURE 2: Cdc42 mobility is reduced at the cell pole where it is organized in large, scaffold-dependent nanoclusters. (A) High-density mEOS-Cdc42 trajectories in live WT and *bem1*Δ cells computed by sptPALM. Scale bar: 2 µm. Different colored trajectories show individual mEOS-Cdc42 proteins that were reconstructed from 20,000 images. Trajectories longer than 10 frames are shown. Insets show a zoom of the cell pole. Insets show mEOS-Cdc42 after 491-nm laser excitation to identify global protein organization. (B) *D* coefficients of different strains and different regions (in box plots displaying the median as a line, the 25th–75th percentiles, and the mean ±SEM) were compared using a nonparametric, two-tailed Mann–Whitney rank sum test. The resulting *P* values are indicated as follows: ns, $P > 0.05$; *, $P < 0.05$; **, $P < 0.01$; ***, $P < 0.001$; ****, $P < 0.0001$. WT *BEM1* cells ($N = 11$ cells; nonpole: $n = 2608$ trajectories; pole: $n = 1021$ trajectories); *bem1*Δ cells ($N = 11$ cells; nonpole: $n = 2200$ trajectories; pole: $n = 1418$ trajectories), and

promoter. These results indicate that the scaffold Bem1 is required for the dynamic range of diffusion displayed by Cdc42 in living cells, and that the slower diffusing cohort within this range reflects Cdc42-GTP, the active form of the GTPase.

We next examined whether the reduced mobility of mEOS-Cdc42 at the pole may reflect its organization in nanoclusters, because Ras and Rac1 nanoclustering is linked to GTPase activity, whereas the nanoscale organization of Cdc42 has not previously been reported (Murakoshi *et al.*, 2004; Plowman *et al.*, 2005; Das *et al.*, 2015; Remorino *et al.*, 2017). mEOS-Cdc42 clustering was investigated by PALM and SR-Tesseler analysis in fixed wild-type cells. We observed that mEOS-Cdc42 nanoclusters were larger at the pole than elsewhere in the cell (median diameter 73 nm ± 2.9 nm [SEM] at the pole vs. 63 nm ± 1.2 nm [SEM] at the nonpole). This larger pool of nanoclusters at the pole was also dependent upon *BEM1* (in *bem1*Δ cells, median diameter 50 nm ± 3 nm [SEM] at the pole vs. 52 nm ± 1.4 nm [SEM] at the nonpole; Figure 2, C and D [chart] and Table 2), consistent with previous work demonstrating that Bem1 contributes directly to Cdc42 activation (Smith *et al.*, 2013; Rapali *et al.*, 2017). Moreover, Cdc42-GTP produced by the *cdc42*-Q61L mutant was organized in nanoclusters at the pole that were larger than those in wild-type cells (median diameter 81 nm ± 2.4 nm [SEM] at the pole for Cdc42-GTP vs. 74 nm ± 2.9 nm [SEM] for wild-type cells; Figure 2, E and F and Table 2). We also observed larger nanoclusters of Cdc42 at the pole when tagged with mEOS3.2, a fluorophore that was engineered to obviate dimerization, thus serving as a control that Cdc42 nanoclustering was not induced by the mEOS tag (median diameter mEOS3.2-Cdc42 73 nm ± 3.6 nm [SEM] at the pole vs. 56 nm ± 1.7 nm [SEM] at the nonpole; Table 2; Zhang *et al.*, 2012). Collectively, these results provide direct evidence that Cdc42 exhibits heterogeneous diffusion, displaying reduced mobility at the cell pole. The reduction in mobility of Cdc42 at the pole reflects its organization in nanoclusters whose size correlates with active GTPase.

The organization of active K-Ras and H-Ras in nanoclusters has also previously been reported, which, together with our results, suggest that activity-dependent nanoclustering may be a general feature of Ras-related GTPases (Murakoshi *et al.*, 2004; Plowman *et al.*, 2005; Remorino *et al.*, 2017). Previous work also indicated a role for phosphatidylserine (PS) in the regulation of K-Ras GTPase signaling via nanoclustering (Zhou *et al.*, 2014, 2015; Cho *et al.*, 2016). PS also plays an important, yet incompletely understood role in the recruitment of Cdc42 to the cell pole in budding and fission yeast (Fairn *et al.*, 2011; Haupt and Minc, 2017). Consistently, PS is enriched in regions of the plasma membrane where Cdc42 also localizes (Fairn *et al.*, 2011; Slaughter *et al.*, 2013). Reasoning that PS is therefore likely to contribute to Cdc42 signaling and nanoclustering, we modulated the levels of this phospholipid in the plasma membrane and examined its effect on mEOS-Cdc42 organization. Plasma membrane PS levels at the cell pole were increased by deleting the two PS decarboxylases *PSD1* and *PSD2* that convert PS to phosphatidylethanolamine (PE) (Horvath *et al.*, 2011), resulting in increased recruitment of a PS probe to the plasma membrane (Supplemental Figure S2A; Fairn *et al.*, 2011). Having verified that levels of active Cdc42 and Bem1 were increased in the *psd1*Δ *psd2*Δ (Supplemental Figure S2B), we quantified mEOS-Cdc42 clustering by PALM and SR-Tesseler (Figure 3A). In this double mutant, which also contained untagged Cdc42, we observed that mEOS-Cdc42 was organized in nanoclusters that were larger in diameter at the pole compared with wild-type cells (median 84 nm ± 4.3 nm [SEM] in *psd1*Δ *psd2*Δ cells vs. 74 nm ± 2.9 nm [SEM] in wild-type cells; Figure 3B). However, the sizes of mEOS-Cdc42 nanoclusters were not significantly larger in the nonpole regions of the cell (median 60 nm ± 1.5 nm [SEM] in *psd1*Δ *psd2*Δ and 56 nm ± 1.7 nm [SEM] in wild-type cells; Table 2).

Conversely, to observe Cdc42 organization in cells depleted of PS, we used the *cho1*Δ mutant in which the sole PS synthase in budding yeast is deleted. In this mutant, in which an untagged copy of Cdc42 is also present, only 25% of cells display polarized mEOS-Cdc42 (Figure 3C). The addition of exogenous Lyso-PS increased the fraction of *cho1*Δ cells displaying polarized mEOS-Cdc42 to 57% and increased the levels of active Cdc42 at the cell pole (Figure 3D). Additionally, Lyso-PS resulted in an increase in the median diameter of mEOS-Cdc42 nanoclusters from 52 nm in nonpolarized *cho1*Δ cells to 70 nm ± 4.5 nm (SEM) at the pole of polarizing cells (Figure 3E and Table 2). Although the addition of lyso-phosphatidylcholine (Lyso-PC) to wild-type cells had no effect on the size of mEOS-Cdc42 nanoclusters at the cell pole (median diameter 74 nm ± 2.9 nm [SEM] without Lyso-PC and 71 nm ± 3.9 nm [SEM] with Lyso-PC), the addition of Lyso-PS resulted in the organization of mEOS-Cdc42 into larger nanoclusters (median diameter at the pole 89 nm ± 5 nm [SEM] with Lyso-PS vs. 71 nm ± 3.9 nm [SEM] with Lyso-PC; Figure 3E, Supplemental Figure S2C, and Table 2). These results motivated us to address whether the organization of mEOS-Cdc42 into larger nanoclusters at the pole after the addition of Lyso-PS might be dependent upon Bem1. Strikingly, we observed that the addition of Lyso-PS to *bem1*Δ cells did not result in the organization of mEOS-Cdc42 into larger nanoclusters at the cell pole (median diameter 62 nm ± 1.4 nm [SEM] after Lyso-PS addition at the pole and nonpole in *bem1*Δ cells; Figure 3E and Table 2). These results indicate that Bem1 is required for the organization of mEOS-Cdc42 into the larger nanoclusters observed at the pole upon Lyso-PS addition.

mEOS-cdc42-Q61L cells ($N = 10$ cells; nonpole: $n = 1502$ trajectories; pole: $n = 2001$ trajectories). (C) SR-Tesseler images of mEOS-Cdc42 nanocluster organization in fixed WT *BEM1* and *bem1*Δ cells. Images display 5800 and 5609 localizations for *BEM1* and *bem1*Δ, respectively. A zoom of the pole region outlined by a blue box shows the organization of the detected nanoclusters, colored blue, in the strains indicated. Scale bar in the zoom: 25 nm. Insets show mEOS-Cdc42 after 491 nm widefield laser excitation to identify the cell pole. Scale bar: 2 µm. (D) Distribution of nanocluster area at the pole and nonpole (NP) regions of fixed WT *BEM1* ($N = 10$ cells; nonpole: $n = 625$ clusters; pole: $n = 268$ clusters) and *bem1*Δ cells ($N = 10$ cells; nonpole: $n = 581$ clusters; pole: $n = 130$ clusters). Data are presented as scatter dot plots displaying the median as a line and the 25th–75th percentiles. Data were compared using a nonparametric, two-tailed Mann–Whitney rank sum test. (E) SR-Tesseler images of mEOS-Cdc42 in fixed WT ($N = 10$ cells; nonpole: $n = 268$ clusters; pole: $n = 133$ clusters) and mEOS-cdc42-Q61L ($N = 10$ cells; nonpole: $n = 232$ clusters; pole: $n = 303$ clusters) cells. Images display 2799 and 6152 localizations for mEOS-Cdc42 and mEOS-cdc42-Q61L, respectively. Insets (top left) display mEOS-Cdc42 after 491-nm laser excitation to identify the cell pole. Note that these experiments were carried out after repression of endogenous *CDC42* expressed from the *GAL1* promoter. Insets and nanocluster detections are the same as in C. Scale bar: 2 µm and 25 nm in the zoom. (F) Distribution of nanocluster areas, which were analyzed and represented as in D.

	mEOS3.2-Cdc42		WT		*BEM1*		*bem1Δ*	
	Pole (P)	Nonpole (NP)	P	NP	P	NP	P	NP
Number of clusters	113	171	239	654	137	324	132	583
Median (nm; IQR)	73 (51–95)	56 (41–73)	74 (48–103)	62 (46–83)	73 (48–101)	63 (46–94)	50 (37–72)	52 (38–76)
Mean (nm; SEM)	77 (±3.6)	58 (±1.7)	82 (±2.9)	68 (±1.2)	80 (±3.7)	74 (±2.2)	61 (±3)	61 (±1.4)

	bem1Δ + Lyso-PS		W303		*cdc42* Q61L		*psd1Δpsd2Δ*	
	P	NP	P	NP	P	NP	P	NP
Number of clusters	126	696	137	272	306	130	174	227
Median (nm; IQR)	61 (44–97)	62 (46–87)	68 (48–97)	50 (36–76)	81 (62–115)	70 (50–103)	84 (56–124)	60 (48–78)
Mean (nm; SEM)	74 (±4)	72 (±1.4)	75 (±3.1)	60 (±2)	92 (±2.4)	82 (±4.2)	98 (±4.3)	64 (±1.5)

	WT + Lyso-PS		WT + Lyso-PC		*cho1Δ*			*cho1Δ* + Lyso-PS	
	P	NP	P	NP	All cell	P	NP	P	NP
Number of clusters	99	252	205	353	324	153	355	93	375
Median (nm; IQR)	89 (59–117)	63 (48–81)	71 (47–113)	59 (46–75)	52 (39–67)	65 (43–94)	60 (45–82)	70 (42–99)	61 (43–83)
Mean (nm; SEM)	94 (±5)	67 (±1.7)	85 (±3.9)	62 (±1.3)	53 (±1.1)	73 (±3.3)	66 (±1.5)	76 (±4.5)	65 (±1.5)

	cho1Δ+ Lyso-PC		*PIL1-mEOS*
	P	NP	All cell
Number of clusters	135	462	586
Median (nm; IQR)	64 (48–85)	64 (44–85)	105 (79–141)
Mean (nm; SEM)	68 (±2.4)	68 (±1.4)	115 (±2)

The values displayed are for mEOS-Cdc42 clusters, with the exception of the first data set, which displays mEOS3.2-Cdc42 clusters, and the last data set, which displays Pil1-mEOS clusters.

TABLE 2: Cluster diameter.

The distribution of mEOS-Cdc42 nanocluster sizes was multimodal, displaying subpopulations of three dominant sizes at the pole of wild-type cells (Figure 4A, red line). The smallest and least abundant population was not analyzed further, because it corresponded to the resolution of our imaging system. However, the middle population of nanoclusters had an average diameter of 56 nm ± 5.7 nm (SD) and an area of 2818 nm^2 ± 189 nm^2 (SD). The largest pool of nanoclusters was strongly enriched at the pole, while being virtually absent at the nonpole. In this largest pool, we measured an average diameter of 103 nm ± 11.5 nm (SD) and an area of 11,092 nm^2 ± 189 nm^2 (SD). This pool of largest nanoclusters was increased in cells expressing Cdc42-GTP and in *psd1Δ psd2Δ* mutants, in which PS and active Cdc42 were enriched at the pole (Figure 4, B and C). Moreover, the largest pool of mEOS-Cdc42 nanoclusters was markedly reduced in *bem1Δ* cells (Figure 4D). Cdc42 therefore appears to be organized in nanoclusters of distinct sizes, reflecting the activation of the GTPase, whose proportion varies in different mutants. Given that the area of Cdc42 nanoclusters was observed to increase by a factor of 4 in wild-type cells, and consequently the nanocluster diameter by a factor of 2, we propose that nanoclusters may concatemerize via a mechanism linked to GTPase activation and PS levels. Importantly, we observed little tendency for eisosomes containing Pil1-mEOS to display concatemerization (Supplemental Figure S3), indicating that concatemerization may be specific to Cdc42.

Our sptPALM measurements indicate a less pronounced difference in mobility, *D*, between Cdc42 at the pole and nonpole than that previously reported by iFRAP (we find *D* pole 0.016 $\mu m^2\ s^{-1}$ and *D* nonpole 0.027 $\mu m^2\ s^{-1}$, compared with that reported by iFRAP of *D* pole 0.0061 $\mu m^2\ s^{-1}$ and *D* nonpole 0.053 $\mu m^2\ s^{-1}$ [Slaughter *et al.*, 2013]). We also report an overall reduced mobility of Cdc42 compared with previous FRAP measurements (0.036 $\mu m^2\ s^{-1}$ [Marco *et al.*, 2007]). Thus, the tendency of Cdc42 to display reduced diffusion at the pole is borne out by both sptPALM and iFRAP, but the absolute values are different. The ensemble nature of the measurements in iFRAP and FRAP, combined with their dependency on modeling and fitting, may contribute to the differences in the values obtained using these methods compared with the sptPALM measurements presented in the present study. The sptPALM approach presented here was also sufficiently sensitive to indicate a role for Bem1 in the reduced mobility of Cdc42 at the pole. Previous ensemble measurements did not

identify this effect (Wedlich-Soldner *et al.*, 2004), which may reflect the sensitivity of spt versus ensemble measurements. The inclusion of these and the additional quantitative measurements that we report in this study, will provide experimentally derived parameters for future modeling studies of cellular polarity.

Although Cdc42 has previously been observed in clusters (Ziman *et al.*, 1993; Slaughter *et al.*, 2013), its organization and regulation within subdiffraction-limited domains, or nanoclusters, has not previously been reported. However, other Ras family GTPases including Rac1, H-Ras, and K-Ras have been observed in nanoclusters, whose size is also related to GTPase activation (Murakoshi *et al.*, 2004; Tian *et al.*, 2007; Das *et al.*, 2015; Nan *et al.*, 2015; Remorino *et al.*, 2017). The nanoclustering of proteins at the plasma membrane appears to be an inherent property of many signaling pathways, although fundamental questions regarding the control of nanoclustering remain unexplored (Garcia-Parajo *et al.*, 2014). The observation that signaling proteins such as Cdc42 are organized in nanoclusters raises questions regarding the factors controlling Cdc42 residency times in the nanoclusters, the mobility of the nanoclusters, and their propensity to concatenate, as has been reported for other signaling systems (Lillemeier *et al.*, 2010). Addressing these questions would be facilitated by long-term single-molecule imaging. Regulatory factors such as Bem1 and anionic lipids have the potential to contribute to these dynamic features of signaling via the control of GTPase pathway activity.

MATERIALS AND METHODS

Growth conditions

The yeast strains and plasmids used in this study are listed in Supplemental Table 1, A and B. Yeast were cultivated in defined minimal medium (SC) at 30°C containing 2% dextrose, supplemented with appropriate nutrients to maintain plasmid selection. Cells were diluted to $OD_{600} \approx 0.2$ and grown until midlog phase and then directly imaged or fixed. Media (liquid and solid) were supplemented with 0.5 mM choline (Sigma-Aldrich) or 5 mM ethanolamine (Sigma-Aldrich) to allow the growth of *cho1*Δ cells and *psd1*Δ*psd2*Δ cells, respectively.

Addition of Lyso-PS and Lyso-PC

Lyso-PS and Lyso-PC (Avanti Polar Lipids), dissolved in chloroform, were dried in a centrifugal evaporator, washed with water, and then dried and resuspended in SC media to obtain a final lipid concentration of 55 µM (Maeda *et al.*, 2013). Lipids (1 ml) were incubated with 1 ml of cells for 15–30 min. Cells were then fixed, washed with phosphate-buffered saline (PBS) twice, and imaged.

Yeast strains and plasmid construction

Cdc42 dynamics were analyzed using a strain in which endogenous *CDC42* was deleted (*cdc42::CaURA3*) and *CDC42* function was provided by expression of mEOS-*CDC42* from the *CDC42* promoter on a CEN plasmid (pDM303 in DMY2000 and DMY2023; Rapali *et al.*, 2017). The mEOS-Cdc42 fusion construct contained a short, flexible GAGAGA linker between the fluorophore and Cdc42, which we have found to be important for optimal Cdc42 function. This plasmid was used as a template to generate *cdc42-Q61L* (pDM575) by QuickChange site-directed mutagenesis. For comparison of mEOS-Cdc42 and mEOS-cdc42-Q61L dynamics, a yeast strain in which the endogenous copy of *CDC42* was expressed from the *GAL1* promoter (DMY 2114), was transformed with mEOS-*CDC42* (pDM 303) and mEOS-*cdc42-Q61L* (pDM 575). Transformants that had been grown in 2% galactose were switched to 2% dextrose 4 h before imaging to repress expression of the endogenous *CDC42* gene and enable visualization of mEOS-tagged Cdc42 WT or Q61L.

PIL1-mEOS dynamics were studied by generating a *Pil1-mEOS* strain tagged at the genomic locus (DMY 2290). An mEOS-HIS3MX6 cassette was generated by PCR amplification of a GAGAGA-mEOS sequence and ligation into *Pac*I-*Asc*I–digested pFA6a-GFP(S65T)-HIS3MX6 plasmid (Longtine *et al.*, 1998). The resulting plasmid (pDM574) was used to tag the endogenous copy of *PIL1* with mEOS.

BEM1-yEGFP::CaURA3 was generated by replacing the G418-selectable marker in pFA6a-GFP(S65T)-kanMX6 with *CaURA3* to generate pFA6a-*yEGFP-CaURA3* (pDM874; Longtine *et al.*, 1998). To monitor the in vivo levels of Cdc42-GTP, we generated a $gic2_{(1\text{-}208)}$-yEGFP fusion (*Cyc1p-gic2*$_{(1\text{-}208)}$*-yEGFP* [pDM885]), containing the CRIB motif of Gic2 that was cloned into a modified pRS315 plasmid and expressed from the *CYC1* promoter (pDM850; Curran *et al.*, 2014). Plasmid *mCherry-gic2*$_{(1\text{-}208)}$ (pDM789) was constructed by inserting the *TPI1* promoter into a PRS416 plasmid (*Xho*I-*Hin*dIII) followed by an mCherry sequence (*Hin*dIII-*Eco*RI), *gic2*$_{(1\text{-}208)}$ (*Eco*RI-*Bam*HI), and the *ADH1* terminator (*Not*I).

Calcofluor staining

Live cells in midlog phase were stained for 5 min with 2 µg ml^{-1} calcofluor white and then washed with PBS. Cells were directly imaged under 405-nm laser excitation. Images in Supplemental Figure S1C display maximum projections of 16 z-sections that were deconvolved using a custom-written plug-in running within MetaMorph (Jose *et al.*, 2015).

Pheromone treatment

Shmoo morphology was imaged 90 min after the addition of synthetic α-factor to a liquid culture of midexponential phase cells grown at 30°C. α-Factor was added to 10 µM for *BAR1* strains and 1 µM for *bar1*Δ strains.

The cellular response to α-factor was measured using a growth inhibition, or halo assay, in which cells from an overnight culture were diluted to a final $OD_{600\ nm} \approx 1$ in appropriate selective medium. Cells (10 µl) were mixed with 3 ml of 0.75% (wt/vol) cooled molten agar and immediately poured onto a Petri dish containing the same selective medium. Sterile filter disks (6 mm diameter) were spotted with 0.2 µg α-factor and placed on the plates, which were incubated for 3 d at 30°C.

GFP-LactC2 fluorescence measurement

The average fluorescence intensity of image stacks containing 11 Z-planes was projected and the background signal was subtracted. A region of interest was drawn around the plasma membrane of the pole (which was defined manually) to obtain the mean gray value for each cell. Fluorescence intensity values were then normalized as follows: average mean gray value of *psd1*Δ*psd2*Δ pole/average mean gray value of wild-type pole. The average fluorescence intensity of three independent experiments was plotted using Prism software.

Imaging active Cdc42 using a $gic2_{1\text{-}208}$ fluorescent reporter

Fluorescently tagged $gic2_{1\text{-}208}$ contains a CRIB domain that has been used as a reporter for active Cdc42. The average fluorescence intensity of image stacks containing six Z-planes was projected and the background signal was subtracted. Next, at the pole of the cell, the average fluorescence intensity of the pole (AFIP) and the cytosol (AFIC) were determined by manual segmentation of each cell using ImageJ software. The AFIP was normalized as follows: normalized fluorescence intensity of the pole = (AFIP-AFIC)/AFIC). The values

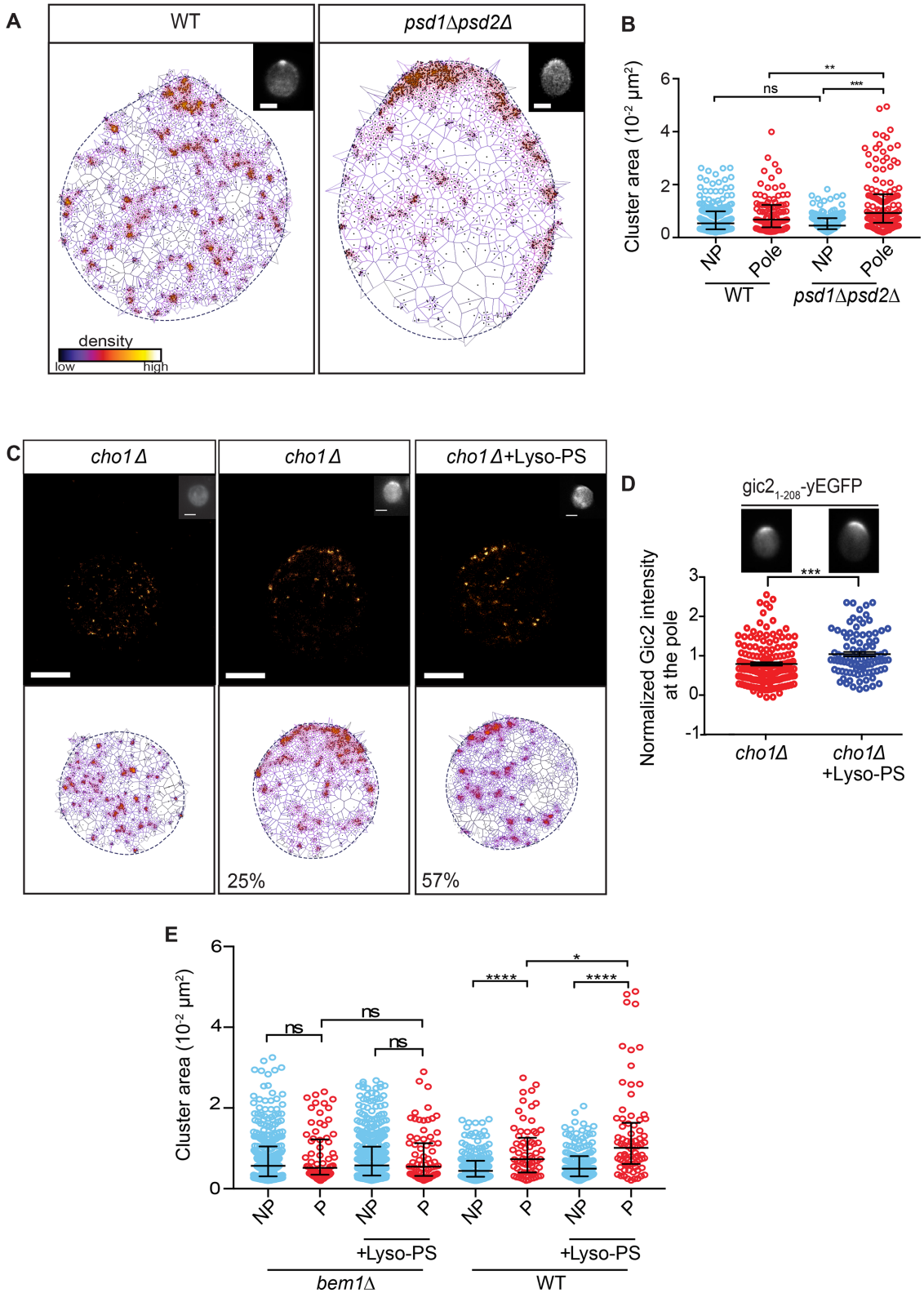

FIGURE 3: Cdc42 nanocluster size is positively regulated by PS in a scaffold-dependent manner. (A) SR-Tesseler image displaying mEOS-Cdc42 nanocluster organization in fixed WT and *psd1*Δ*psd2*Δ cells. Images display 2544 and 4674 detections for WT and *psd1*Δ*psd2*Δ, respectively. Insets (top right) show mEOS-Cdc42 after 491-nm laser excitation to identify the cell pole. Scale bar: 2 µm. A dotted blue line indicates the cell contour. (B) Nanocluster sizes are presented as scatter dot plots displaying the median as a line with the 25th–75th percentiles. Data were compared using a nonparametric, two-tailed Mann–Whitney rank sum test. The graph shows the cluster area of mEOS-Cdc42 in WT and *psd1*Δ*psd2*Δ cells at the pole and nonpole (NP) regions of WT ($N = 9$ cells; nonpole: $n = 313$ clusters; pole $n = 134$ clusters) and *psd1*Δ*psd2*Δ cells ($N = 9$ cells; nonpole: $n = 229$ clusters; pole: $n = 170$ clusters). (C) PALM (top panel) and

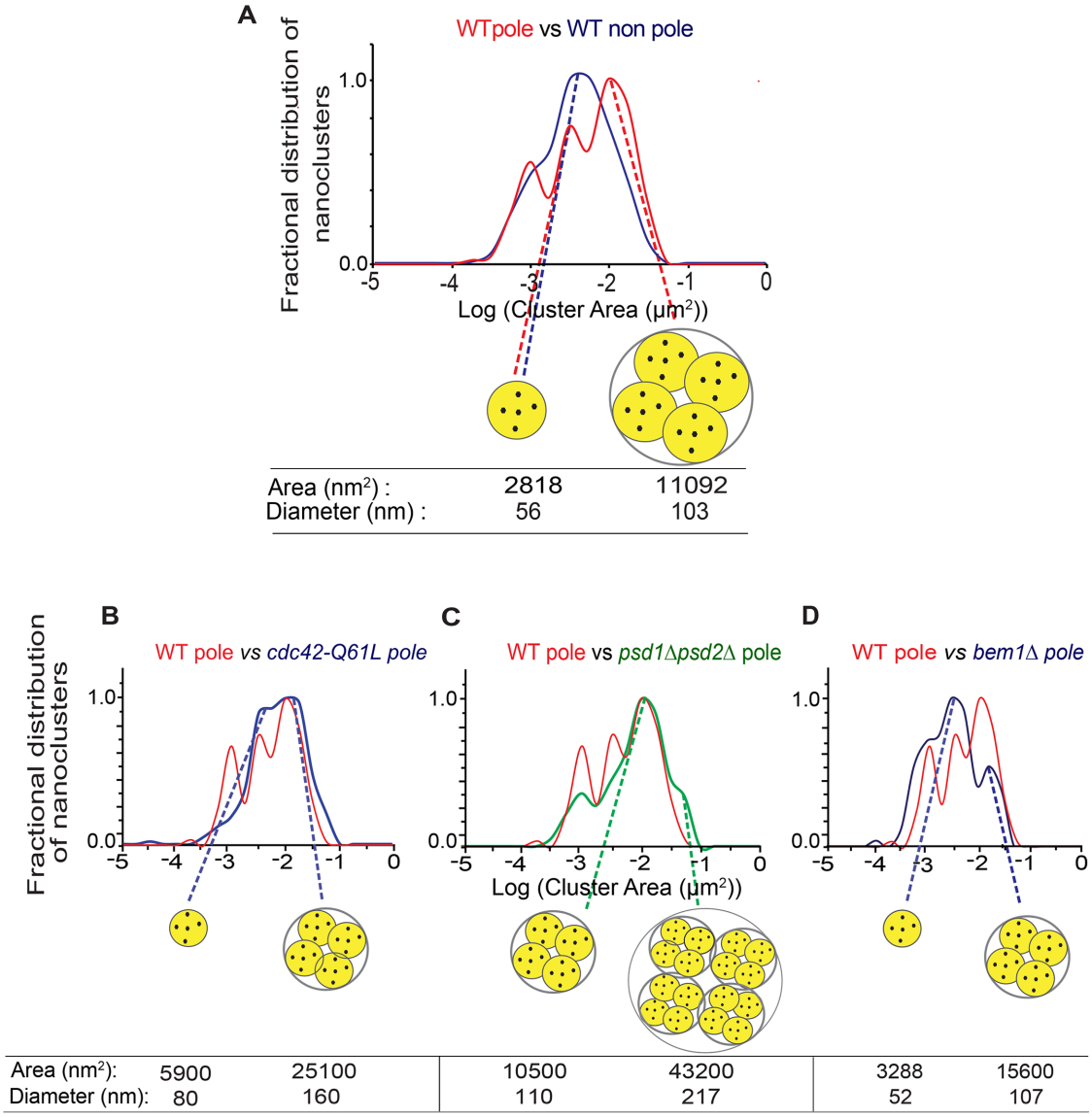

FIGURE 4: PS and Bem1 may influence Cdc42 nanocluster size via nanocluster concatenation. (A) Area distribution of mEOS-Cdc42 nanoclusters in fixed wild-type cells. Note the multimodal distribution. The red line displays the distribution of detected nanoclusters at the pole and the blue line shows the nonpole. Nanocluster area and diameter were extracted as an average of the values around the mode where the bin width is 0.25. (B) Area distribution of Cdc42-GTP (mEOS-*cdc42-Q61L*) nanoclusters at the pole in blue vs. wild-type mEOS-*CDC42* in red from fixed cells. (C) Area distribution of mEOS-Cdc42 nanoclusters at the pole of fixed *psd1*Δ*psd2*Δ cells in green vs. mEOS-*CDC42* nanoclusters at the pole of wild-type cells in red. (D) Area distribution of mEOS-Cdc42 nanoclusters at the pole of fixed *bem1*Δ cells in blue vs. mEOS-*CDC42* nanoclusters at the pole of wild-type cells in red.

SR-Tesseler (bottom panel) images of mEOS-Cdc42 in *cho1*Δ cells and *cho1*Δ cells incubated for 30 min with Lyso-PS, before being fixed. Insets (top right in PALM image) show mEOS-Cdc42 after 491-nm laser excitation to identify the cell pole. The *cho1*Δ cells were mostly unbudded (75%). Only 25% of these unbudded cells display polarized mEOS-Cdc42. Addition of Lyso-PS increased the number of unbudded cells with polarized mEOS-Cdc42 to 57%. A dotted blue line indicates the cell contour. Images display 2869, 2731, and 3503 localizations for *cho1*Δ, polarized *cho1*Δ, and *cho1*Δ+ Lyso-PS, respectively. (D) Active Cdc42 was detected using a $gic2_{1\text{-}208}$-CRIB-YeGFP probe (pDM885) after Lyso-PS treatment of *cho1*Δ cells (*cho1*Δ: $N = 161$ cells; *cho1*Δ+ Lyso-PS: $N = 94$). Lines display mean ± SEM. (E) Distribution of nanocluster area of the pole and nonpole (NP) regions of WT ($N = 10$ cells; nonpole: $n = 325$ clusters; pole $n = 96$ clusters), WT + Lyso-PS ($N = 8$ cells; nonpole: $n = 247$ clusters; pole $n = 97$ clusters), *bem1*Δ cells ($N = 10$ cells; nonpole: $n = 581$ clusters; pole: $n = 130$ clusters), and *bem1*Δ+ Lyso-PS cells ($N = 10$ cells; nonpole: $n = 675$ clusters; pole $n = 121$ clusters). Nanocluster area is presented as scatter dot plots displaying the median as a line and the 25th–75th percentiles. Values were compared using a nonparametric, two-tailed Mann–Whitney rank sum test. The resulting P values are indicated as follows: not significant (ns), $P > 0.05$; *, $P < 0.05$; **, $P < 0.01$; ***, $P < 0.001$; ****, $P < 0.0001$.

were plotted using Prism software. The same procedure was followed to quantify Bem1 at the pole.

sptPALM

Live cells were imaged using a widefield, inverted microscope (Axiovert 200M; Carl Zeiss, Marly le Roi, France) equipped with a 100× TIRFM objective (oil, NA 1.46; Plan Apo), iLas^2 TIRF system (Roper Scientific), and an EMCCD camera (Evolve; Photometrics, Tuscon, Arizona). The imaging system was maintained at a constant temperature of 25°C using a custom-designed incubator (Box and Cube; Life Imaging Services, Basel, Switzerland). MetaMorph 7.7 software (Molecular Devices, Sunnyvale, CA) was used for image acquisition and analysis.

For in vivo imaging, cells expressing mEOS-Cdc42 were grown to midlog phase and imaged at 25°C. Coverslips (high-precision 18 × 18 mm, 1.5 H; Marienfeld, Lauda-Königshofen, Germany) were washed overnight in a solution of 1 M HCl and 1 M HNO_3 and then rinsed three times the next day in ultrapure water. After a 30-min incubation in water and then 30 min in ethanol, the coverslips were dried and used for imaging. Imaging was performed in a highly oblique illumination (HiLo) mode. mEOS-Cdc42 cells were imaged using a 561-nm laser with additional continuous photoconversion using a 405-nm laser. The 405-nm laser was maintained at low power (0.3–1 μW) for adequate separation of stochastically converted molecules. The iLas^2 system was used in arc mode for live imaging and ellipse mode for fixed samples. These settings set the pattern of rotation of the lasers on the back focal plane of the TIRF objective. The fluorescence was collected on the EMCCD camera after passing through a combination of dichroic and emission filters (D101-R561 and F39-617, respectively; Chroma, Bellows Falls, VT). Images were acquired in streaming mode at 50 Hz (20-ms exposure time). During in vivo imaging, 16,000–20,000 images were collected for each cell. Multicolor fluorescent 100-nm beads (Tetraspeck; Invitrogen) were used as fiduciary markers in all superresolution imaging experiments to register long-term acquisitions for lateral drift correction.

For fixed-cell imaging, cells were grown to log phase ($OD_{600\ nm}$ of <0.8) and fixed with 3.7% formaldehyde and 0.2% glutaraldehyde for 10 min. After being washed in PBS three times, cells were resuspended in PBS and directly used for imaging. Image acquisition of fixed cells was performed using the same protocol as for living cells, as described above. Images (32,000–40,000) were acquired per cell, at which point the pool of photoconvertible single molecules was completely depleted.

Single-particle localization, tracking, and nanocluster detection by Voronoi tessellation

Image stacks collected for each sptPALM experiment were analyzed using custom-written software operating as a plug-in within MetaMorph software, PalmTracer, to compute single-molecule localizations and dynamics. Diffusion coefficients obtained for each strain are listed in Table 1. Single molecules were localized in each image frame and tracked over time using wavelet segmentation and simulated annealing algorithms (Racine *et al*., 2007; Izeddin *et al*., 2012). The sptPALM image resolution, defined as FWHM = 2.3× the pointing accuracy, was estimated to 48 nm. The pointing accuracy, measured to be 20.86 nm, was computed from the acquisition of mEOS-Cdc42 in fixed cells by bidimensional Gaussian fitting of the spatial distribution of 80 single molecules localized for more than 20 consecutive time points. Tracking data and subsequent MSDs were generated from the membrane-bound population of mEOS-Cdc42. Proteins in the freely diffusing cytosolic pool of mEOS-Cdc42 were not tracked in these experiments because cytosolic diffusion is much higher than diffusion in a membrane environment and would not be localized and tracked with 20 ms exposure time.

In our observations, all MSDs have a quasilinear dependence at short times, enabling computation of the instantaneous diffusion coefficient (*D*) per molecule by linear regression on the first four points of the MSD of all trajectories that are longer than six consecutive frames.

Cdc42 nanoclusters were quantified from the reconstructed superresolution images of fixed cells using SR-Tesseler analysis (Levet *et al.*, 2015). This software is based on Voronoi tessellation, wherein single-molecule localizations are treated as seeds around which polygons are assembled. In our analysis, we defined regions of interest (ROI) as the pole or nonpole of the cell after visual inspection of the widefield 491-nm image acquired at the outset of the experiment. The surface area of the polygon drawn around the detected single molecule is proportional to the local molecular density, such that the area of the polygon decreases as the local density of single-molecule localizations increases. PALM images were corrected for single-molecule blinking within the SR-Tesseler software (Levet *et al*., 2015). This takes into account mEOS photophysics and a pointing accuracy of 20 nm as a radius of search, which would otherwise overestimate the number of single-molecule detections. After blinking correction, nanoclusters were defined as those areas containing a minimum of five localizations at a local density that was at least twofold higher than the average density within the selected ROI. Nanocluster characteristics including diameter, area, and the number of localizations were exported from SR-Tesseler into Excel (Microsoft) for further statistical analysis.

Statistical analysis

The diffusion coefficients were represented as box plots displaying the median as a line and the percentiles (25–75%). Statistical comparisons were made using a nonparametric, two-tailed Mann–Whitney rank sum test. Non-Gaussian distributions of nanocluster sizes were represented by data points displaying median as a line and the percentiles (25–75%) and also compared using a nonparametric, two-tailed Mann–Whitney rank sum test. Statistical analyses were based on cluster area values calculated by SR-Tesseler. Only areas greater than 2000 nm^2 were used, corresponding to a diameter of 48 nm, the resolution of our imaging system.

ACKNOWLEDGMENTS

We thank Jeremy Thorner and Günther Daum for yeast strains and Sylvain Tollis and Deepak Nair for performing a preliminary analysis of Cdc42 dynamics. We also thank Anne Royou for comments on the manuscript and Florian Levet and Anne Beghin for help with SR-Tesseler analysis. This project received funding from the European Union's Horizon 2020 research and innovation program under the Marie Sklodowska-Curie Grant agreement no. 708972—"Lipids and Polarity." The work was also funded by the Centre National de la Recherche Scientifique, Agence Nationale pour la Recherche through Program Blanc Grant no. ANR-13-BSV2-0015-01, the University of Bordeaux Synthetic Biology (SB2) Program, and the Regional Council of Aquitaine.

REFERENCES

Adams AE, Johnson DI, Longnecker RM, Sloat BF, Pringle JR (1990). CDC42 and CDC43, two additional genes involved in budding and the establishment of cell polarity in the yeast *Saccharomyces cerevisiae*. J Cell Biol 111, 131–142.

Bastos RN, Penate X, Bates M, Hammond D, Barr FA (2012). CYK4 inhibits Rac1-dependent PAK1 and ARHGEF7 effector pathways during cytokinesis. J Cell Biol 198, 865–880.

Bement WM, von Dassow G (2014). Single cell pattern formation and transient cytoskeletal arrays. Curr Opin Cell Biol 26, 51–59.
Bendezu FO, Vincenzetti V, Vavylonis D, Wyss R, Vogel H, Martin SG (2015). Spontaneous Cdc42 polarization independent of GDI-mediated extraction and actin-based trafficking. PLoS Biol 13, e1002097.
Benink HA, Bement WM (2005). Concentric zones of active RhoA and Cdc42 around single cell wounds. J Cell Biol 168, 429–439.
Bianchi F, Syga L, Moiset G, Spakman D, Schavemaker PE, Punter CM, Seinen AB, van Oijen AM, Robinson A, Poolman B (2018). Steric exclusion and protein conformation determine the localization of plasma membrane transporters. Nat Commun 9, 501.
Cho KJ, van der Hoeven D, Zhou Y, Maekawa M, Ma X, Chen W, Fairn GD, Hancock JF (2016). Inhibition of acid sphingomyelinase depletes cellular phosphatidylserine and mislocalizes K-Ras from the plasma membrane. Mol Cell Biol 36, 363–374.
Curran KA, Crook NC, Karim AS, Gupta A, Wagman AM, Alper HS (2014). Design of synthetic yeast promoters via tuning of nucleosome architecture. Nat Commun 5, 4002.
Das S, Yin T, Yang Q, Zhang J, Wu YI, Yu J (2015). Single-molecule tracking of small GTPase Rac1 uncovers spatial regulation of membrane translocation and mechanism for polarized signaling. Proc Natl Acad Sci USA 112, E267–E276.
Fairn GD, Hermansson M, Somerharju P, Grinstein S (2011). Phosphatidylserine is polarized and required for proper Cdc42 localization and for development of cell polarity. Nat Cell Biol 13, 1424–1430.
Freisinger T, Klunder B, Johnson J, Muller N, Pichler G, Beck G, Costanzo M, Boone C, Cerione RA, Frey E, Wedlich-Soldner R (2013). Establishment of a robust single axis of cell polarity by coupling multiple positive feedback loops. Nat Commun 4, 1807.
Garcia-Parajo MF, Cambi A, Torreno-Pina JA, Thompson N, Jacobson K (2014). Nanoclustering as a dominant feature of plasma membrane organization. J Cell Sci 127, 4995–5005.
Giese W, Eigel M, Westerheide S, Engwer C, Klipp E (2015). Influence of cell shape, inhomogeneities and diffusion barriers in cell polarization models. Phys Biol 12, 066014.
Goryachev AB, Pokhilko AV (2008). Dynamics of Cdc42 network embodies a Turing-type mechanism of yeast cell polarity. FEBS Lett 582, 1437–1443.
Haupt A, Minc N (2017). Gradients of phosphatidylserine contribute to plasma membrane charge localization and cell polarity in fission yeast. Mol Biol Cell 28, 210–220.
Horvath SE, Wagner A, Steyrer E, Daum G (2011). Metabolic link between phosphatidylethanolamine and triacylglycerol metabolism in the yeast *Saccharomyces cerevisiae*. Biochim Biophys Acta 1811, 1030–1037.
Izeddin I, Boulanger J, Racine V, Specht CG, Kechkar A, Nair D, Triller A, Choquet D, Dahan M, Sibarita JB (2012). Wavelet analysis for single molecule localization microscopy. Opt Express 20, 2081–2095.
Jose M, Tollis S, Nair D, Mitteau R, Velours C, Massoni-Laporte A, Royou A, Sibarita JB, McCusker D (2015). A quantitative imaging-based screen reveals the exocyst as a network hub connecting endo- and exocytosis. Mol Biol Cell 26, 2519–2534.
Jose M, Tollis S, Nair D, Sibarita JB, McCusker D (2013). Robust polarity establishment occurs via an endocytosis-based cortical corralling mechanism. J Cell Biol 200, 407–418.
Kabeche R, Baldissard S, Hammond J, Howard L, Moseley JB (2011). The filament-forming protein Pil1 assembles linear eisosomes in fission yeast. Mol Biol Cell 22, 4059–4067.
Le Floc'h A, Tanaka Y, Bantilan NS, Voisinne G, Altan-Bonnet G, Fukui Y, Huse M (2013). Annular PIP3 accumulation controls actin architecture and modulates cytotoxicity at the immunological synapse. J Exp Med 210, 2721–2737.
Levet F, Hosy E, Kechkar A, Butler C, Beghin A, Choquet D, Sibarita JB (2015). SR-Tesseler: a method to segment and quantify localization-based super-resolution microscopy data. Nat Methods 12, 1065–1071.
Lillemeier BF, Mortelmaier MA, Forstner MB, Huppa JB, Groves JT, Davis MM (2010). TCR and Lat are expressed on separate protein islands on T cell membranes and concatenate during activation. Nat Immunol 11, 90–96.
Lin WC, Iversen L, Tu HL, Rhodes C, Christensen SM, Iwig JS, Hansen SD, Huang WY, Groves JT (2014). H-Ras forms dimers on membrane surfaces via a protein-protein interface. Proc Natl Acad Sci USA 111, 2996–3001.
Longtine MS, McKenzie A, DeMarini D, Shah NG, Wach A, Brachat A, Philippsen P, Pringle JR (1998). Additional modules for versatile and economical PCR-based gene deletion and modification in *Saccharomyces cerevisiae*. Yeast 14, 953–961.
Maeda K, Anand K, Chiapparino A, Kumar A, Poletto M, Kaksonen M, Gavin AC (2013). Interactome map uncovers phosphatidylserine transport by oxysterol-binding proteins. Nature 501, 257–261.
Manley S, Gillette JM, Patterson GH, Shroff H, Hess HF, Betzig E, Lippincott-Schwartz J (2008). High-density mapping of single-molecule trajectories with photoactivated localization microscopy. Nat Methods 5, 155–157.
Marco E, Wedlich-Soldner R, Li R, Altschuler SJ, Wu LF (2007). Endocytosis optimizes the dynamic localization of membrane proteins that regulate cortical polarity. Cell 129, 411–422.
Monks CR, Freiberg BA, Kupfer H, Sciaky N, Kupfer A (1998). Three-dimensional segregation of supramolecular activation clusters in T cells. Nature 395, 82–86.
Murakoshi H, Iino R, Kobayashi T, Fujiwara T, Ohshima C, Yoshimura A, Kusumi A (2004). Single-molecule imaging analysis of Ras activation in living cells. Proc Natl Acad Sci USA 101, 7317–7322.
Nan X, Tamguney TM, Collisson EA, Lin LJ, Pitt C, Galeas J, Lewis S, Gray JW, McCormick F, Chu S (2015). Ras-GTP dimers activate the Mitogen-Activated Protein Kinase (MAPK) pathway. Proc Natl Acad Sci USA 112, 7996–8001.
Orlando K, Sun X, Zhang J, Lu T, Yokomizo L, Wang P, Guo W (2011). Exo-endocytic trafficking and the septin-based diffusion barrier are required for the maintenance of Cdc42p polarization during budding yeast asymmetric growth. Mol Biol Cell 22, 624–633.
Plowman SJ, Muncke C, Parton RG, Hancock JF (2005). H-ras, K-ras, and inner plasma membrane raft proteins operate in nanoclusters with differential dependence on the actin cytoskeleton. Proc Natl Acad Sci USA 102, 15500–15505.
Racine V, Sachse M, Salamero J, Fraisier V, Trubuil A, Sibarita JB (2007). Visualization and quantification of vesicle trafficking on a three-dimensional cytoskeleton network in living cells. J Microsc 225, 214–228.
Rao M, Mayor S (2014). Active organization of membrane constituents in living cells. Curr Opin Cell Biol 29, 126–132.
Rapali P, Mitteau R, Braun C, Massoni-Laporte A, Unlu C, Bataille L, Arramon FS, Gygi SP, McCusker D (2017). Scaffold-mediated gating of Cdc42 signalling flux. eLife 6, e25257.
Remorino A, De Beco S, Cayrac F, Di Federico F, Cornilleau G, Gautreau A, Parrini MC, Masson JB, Dahan M, Coppey M (2017). Gradients of Rac1 nanoclusters support spatial patterns of Rac1 signaling. Cell Rep 21, 1922–1935.
Rittinger K, Walker PA, Eccleston JF, Smerdon SJ, Gamblin SJ (1997). Structure at 1.65 A of RhoA and its GTPase-activating protein in complex with a transition-state analogue. Nature 389, 758–762.
Roos J, Kelly RB (1999). The endocytic machinery in nerve terminals surrounds sites of exocytosis. Curr Biol 9, 1411–1414.
Slaughter BD, Unruh JR, Das A, Smith SE, Rubinstein B, Li R (2013). Non-uniform membrane diffusion enables steady-state cell polarization via vesicular trafficking. Nat Commun 4, 1380.
Smith SE, Rubinstein B, Mendes Pinto I, Slaughter BD, Unruh JR, Li R (2013). Independence of symmetry breaking on Bem1-mediated autocatalytic activation of Cdc42. J Cell Biol 202, 1091–1106.
Tian T, Harding A, Inder K, Plowman S, Parton RG, Hancock JF (2007). Plasma membrane nanoswitches generate high-fidelity Ras signal transduction. Nat Cell Biol 9, 905–914.
Tokunaga M, Imamoto N, Sakata-Sogawa K (2008). Highly inclined thin illumination enables clear single-molecule imaging in cells. Nat Methods 5, 159–161.
Trimble WS, Grinstein S (2015). Barriers to the free diffusion of proteins and lipids in the plasma membrane. J Cell Biol 208, 259–271.
Wahl S, Katiyar R, Schmitz F (2013). A local, periactive zone endocytic machinery at photoreceptor synapses in close vicinity to synaptic ribbons. J Neurosci 33, 10278–10300.
Walther TC, Brickner JH, Aguilar PS, Bernales S, Pantoja C, Walter P (2006). Eisosomes mark static sites of endocytosis. Nature 439, 998–1003.
Wedlich-Soldner R, Wai SC, Schmidt T, Li R (2004). Robust cell polarity is a dynamic state established by coupling transport and GTPase signaling. J Cell Biol 166, 889–900.
Woods B, Kuo CC, Wu CF, Zyla TR, Lew DJ (2015). Polarity establishment requires localized activation of Cdc42. J Cell Biol 211, 19–26.
Yokosuka T, Kobayashi W, Sakata-Sogawa K, Takamatsu M, Hashimoto-Tane A, Dustin ML, Tokunaga M, Saito T (2008). Spatiotemporal regulation of T cell costimulation by TCR-CD28 microclusters and protein kinase C θ translocation. Immunity 29, 589–601.
Yu B, Martins IR, Li P, Amarasinghe GK, Umetani J, Fernandez-Zapico ME, Billadeau DD, Machius M, Tomchick DR, Rosen MK (2010). Structural and energetic mechanisms of cooperative autoinhibition and activation of Vav1. Cell 140, 246–256.

Zhang M, Chang H, Zhang Y, Yu J, Wu L, Ji W, Chen J, Liu B, Lu J, Liu Y, *et al* (2012). Rational design of true monomeric and bright photoactivatable fluorescent proteins. Nat Methods 9, 727–729.

Zhang X, Ma C, Miller AL, Katbi HA, Bement WM, Liu XJ (2008). Polar body emission requires a RhoA contractile ring and Cdc42-mediated membrane protrusion. Dev Cell 15, 386–400.

Zhou Y, Liang H, Rodkey T, Ariotti N, Parton RG, Hancock JF (2014). Signal integration by lipid-mediated spatial cross talk between Ras nanoclusters. Mol Cell Biol 34, 862–876.

Zhou Y, Wong CO, Cho KJ, van der Hoeven D, Liang H, Thakur DP, Luo J, Babic M, Zinsmaier KE, Zhu MX, *et al* (2015). SIGNAL TRANSDUCTION. Membrane potential modulates plasma membrane phospholipid dynamics and K-Ras signaling. Science 349, 873–876.

Ziman M, Preuss D, Mulholland J, O'Brien JM, Botstein D, Johnson DI (1993). Subcellular localization of Cdc42p, a *Saccharomyces cerevisiae* GTP- binding protein involved in the control of cell polarity. Mol Biol Cell 4, 1307–1316.